Probing near-surface atmospheric turbulence with high-resolution lidar measurements and models

C.-Y. J. Kao[1], D. I. Cooper[1], J. M. Reisner[1], W. E. Eichinger[2]

and M. Ghil[3]

Journal of Geophysical Research, (Accepted)

April, 2001

[1]Earth and Environmental Sciences Division, Los Alamos National Laboratory

[2]Iowa Institute for Hydraulic Research, University of Iowa

[3]Department of Atmospheric Sciences and Institute of Geophysics and Planetary Physics, University of California at Los Angeles

ABSTRACT

Lidar technology provides fast data collection at a resolution of meters in a three-dimensional atmospheric volume. A modeling counterpart of this lidar capability can greatly enhance our understanding of near-surface atmospheric turbulence. This paper describes an integrated research capability based on data from a scanning water vapor lidar and a high-resolution hydrodynamic model (HIGRAD) equipped with a visualization routine (VIEWER) that simulates the lidar scanning. The purpose is to better understand the degree to which the lidar measurements represent faithfully the atmospheric boundary layer's spatial and temporal features and to extend the measurements' utility in studying turbulent fields in this layer. Raman lidar water vapor data collected over the Pacific warm pool and the HIGRAD simulations thereof are first compared with each other. The results are then used to identify the potential aliasing effects of lidar measurements due to the relatively long duration of the lidar scanning. This integrated lidar-model capability also helps improve the trade-off between the spatial and temporal resolution of the lidar measurements, on the one hand, and their coverage, on the other.

1. Introduction

Lidar (Light Detection and Ranging) remote sensing (Clifford et al., 1994) offers the promise of multi-dimensional atmospheric measurements for ranges of single to tens of kilometers, with spatial resolution of a few meters. This technology provides measurements to describe atmospheric boundary layer (ABL) phenomena (e.g., Eloranta and Forrest, 1992; Cooper et al., 1994) and to validate advanced models of such phenomena (Avissar et al., 1998; Kao et al., 2000). The lidar system used for the present study is a self-contained field-deployable UV Raman water-vapor lidar (Eichinger et al., 1994) built at the Los Alamos National Laboratory (LANL) and based on the technique pioneered by Melfi et al. (1969). Melfi and colleagues suggested comparing the back-scattered intensities for water and nitrogen in the vibrational Raman band. This permits one to infer the water-vapor concentration, since nitrogen is well mixed in the atmosphere and its concentration is well known.

Water, in its three phases, is of paramount importance in most atmospheric processes: it is involved in feedback mechanisms whose competition affects the climate system on all scales. The surface-atmosphere exchange of water, in particular, has received significantly increased attention. However, a fully quantitative understanding of the near-surface distribution of water vapor has yet to be obtained. A basic problem that remains is to determine the water-vapor distribution at the scale of turbulent eddies (Lawford, 1996). One related problem is the estimation of spatially distributed latent heat flux (or evapotranspiration) over an inhomogeneous surface. The satellite-based data sets upon

which present global environmental assessments depend cannot answer these questions due to its spatial resolution and neither can conventional ground-based point sensors or aircraft measurements. Point sensors near the surface are limited in value because of its small footprint size. It is also due to our current inability to extend the measured values at a point to an understanding of the processes that are occurring on larger scales. The eddy correlation method has been applied to aircraft data for large areas, but it has been called into questions when spatially resolved fluxes are desired (e.g., Mahrt, 1998).

The above-mentioned problems can be mitigated by a scanning lidar because of its high spatial and temporal resolution and the horizontal and vertical cross-sections it can produce. The LANL water vapor lidar system has a spatial resolution of about 1.5 m over a distance of 700 m. It uses an excimer laser source with 400 mJ/pulse of energy at 200 Hz and wavelengths of 248 nm and 351 nm, respectively, for daytime and nighttime operations. The unique receiver uses a 24" f8 telescope and scanning optics to allow three-dimensional volumetric imaging of water-vapor mixing ratio. The receiving detector system provides simultaneous measurement of the elastic back-scattered UV radiation from aerosols and clouds, as well as the nitrogen and water Raman signatures. Field applications of the LANL Raman lidar have been successful over both ocean and land surfaces in helping understand the water vapor's variability and in estimating its surface flux.

Among many recent lidar field experiments conducted by LANL, the Central Equatorial Pacific Experiment (CEPEX) and the Combined Sensor Program (CSP), both over the

Pacific warm pool, are briefly described here. CEPEX was part of an international climate research effort to address the "thermostat hypothesis," a feedback mechanism between water vapor and ocean sea surface temperature purported to limit global warming (Ramanathan and Collins, 1991). Our lidar results during CEPEX show the agreement with the coincident radiosonde water-vapor data within 0.25 g kg^{-1} (Cooper et al., 1996). The CSP project (Post et al., 1997) employed a whole suite of meteorological sensors to quantify processes associated with ocean-atmosphere interactions in the tropics, and to help understand the small-scale processes in the ocean-atmosphere exchange of water and heat. The lidar data shown in this paper were collected during CSP on 26 March 1996. Cooper et al. (1997) and Hagelberg et al. (1998) have shown that the LANL lidar system is a highly accurate and reliable probe of turbulent ABL processes during CSP. However, to better help describe and understand these processes, we need to demonstrate the actual representativeness, as opposed to the mere quantitative accuracy of the lidar data.

Like all volume-imaging sensor systems, lidars require an advanced methodology to make the best use of their measurements' temporal and spatial properties. Over the last decade, experimentalists have made every effort to make the lidar scan as fast as its laser power and detector's efficiency allow, while retaining a good signal-to-noise ratio. This study uses a state-of-the-art turbulence-resolving model to help synthesize the ABL phenomena observed during the CSP experiment through the LANL scanning Raman water-vapor lidar system. We first simulate the formation and evolution of water vapor plumes at comparable spatial and temporal resolution under the meteorological

conditions suggested by rawinsondes and ship measurements. We then "observe" our 4-dimensional model output with a modeled scanning configuration using the actual lidar scanning specifications. The purpose is to validate the structure and quantification of the lidar measured water vapor field, and to investigate the potential aliasing effects of lidar measurements. At the end, a future direction in the integration of lidar measurements and dynamical modeling in terms of data assimilation is described.

2. Lidar Data

In general, the oceanic ABL is characterized by the presence of both vertical wind shear and thermal instability (Stull, 1988). As a result, it can be subdivided into a surface layer, a free-convection layer, and a mixed layer; in each of these sub-layers, the balance of heat, momentum, and moisture fluxes is different. The characteristic height of the surface layer is the Monin-Obukhov (Kaimal and Finnigan, 1994) length of a few tens of meters. The free-convection layer extends up to about 0.1 Z_{in}, where Z_{in} is the height of the first temperature inversion at about 1 km above the surface; Z_{in} is also the characteristic height of the mixed layer. Field experiments using aircraft (William and Hacker, 1993) and numerical studies (Khanna and Brasseur, 1998) show, in fact, that these sub-layers are not well separated from each other. Small-scale plumes formed in the surface layer rise and combine into larger-scale thermals in the free-convection layer, while sinking air from the mixed layer penetrates into the free-convection and surface layers.

When a lidar operates at a fixed azimuth angle and scans over a range in elevation with time, the resultant image covers a vertical slice of the atmosphere (see Fig. 1A). At a fixed height with a zero elevation angle, the lidar can be operated to scan over a horizontal slice of the atmosphere (see Fig. 1B). Neither of the above slices represent a truly instantaneous field of water vapor, simply because each lidar line-of-sight collects data at a different instant in time.

The water-vapor mixing ratio shown in Fig. 1A is a portion of a vertical slice observed during the CSP project. The slice covers 40 degrees of elevation angle and is made up of 81 lines-of-sight, with an angular resolution of 0.5 deg. Each line-of-sight took 0.75 s and the total scanning time was 60 s. The 0.75-s delay between scans and the total scanning time of 60 s should not affect the general flow features being observed: the rising motion of moist air (in red, yellow, and green) and the descending motion of dry air (in purple and blue). But, the spatial structure of the resulting mixed-layer eddies may be aliased if the total duration of the scan is considerably longer.

The regrouping of near-surface coherent plumes into larger and more organized eddies as they rise through the surface layer and the accompanying descent of dry eddies from the well-mixed layer toward the surface have been proposed by earlier studies (Wyngaard, 1988; William and Hacker, 1993). Such organized exchanges between the surface layer and the rest of the ABL above contradict the classical Monin-Obuhkov similarity theory (Kaimal and Finnigan, 1994), which assumes the two to be independent of each other. Simple curve fitting of the data contained in Fig. 1A in comparison with the curve

predicted by the Monin-Obuhkov similarity theory reveals that the theory consistently overestimates the moisture in the upper part of the surface layer because it neglects the drying effect due to the downward motion.

Figure 1B shows the horizontal distribution of water-vapor mixing ratio measured by the lidar at a 10-m elevation above sea level during CSP, based on the same measurement specifications used in Fig. 1A. Using a two-dimensional wavelet technique, Hagelberg et al. (1998) identified a dominant radius of 10 m for the coherent eddies (in red and yellow) shown here in Fig. 1B. The drying effects due to the organized downward airflow (in purple and blue) are also present in the figure.

The total scanning time of 60 s used in constructing Fig. 1B may, however, introduce some aliasing effects in the number and position of small-scale turbulent water-vapor plumes near the surface. This is because the plumes' recycling time scale at the 10-m level is about 10 s, based on the lidar time-series measurements at a fixed point. Since the total scanning time is governed by the 0.75-s delay between scans for a fixed spatial resolution, it suggests that a faster scanning may help to avoid the potential aliasing effects. To provide a more rigorous interpretation of lidar images such as those in Fig.1, we use a hydrodynamic modeling approach to see to what extent lidar imagery does correctly represent ABL turbulence.

3. Model and Simulation Design

The hydrodynamic model used for the current study is an outgrowth of the numerical modeling framework of Smolarkiewicz and Margolin (1993). It is based on a nonoscillatory forward-in-time advection scheme that has the advantage of preserving local extrema, as well as the sign of the transported scalar properties. The scheme has been shown to yield numerical solutions that are consistent with known analytic properties of the modeled flows (Smolarkiewicz and Margolin, 1998). The model minimizes the need for artificial viscosity, while suppressing nonlinear computational instabilities. Overall, the model is designed to accurately simulate small-scale atmospheric dynamics with high-gradient features; hence it is referred to as HIGRAD. A radiation package is included in the model to simulate the radiative effects in the atmosphere (Smith and Kao, 1996).

The effective range of the existing LANL water-vapor lidar is from 100 to 650 m; over this range the nitrogen and water-vapor signals coincide, thus insuring the accuracy of the measurements. In order to match the lidar's effective range, we use a three-dimensional model domain with a size of 560 m by 560 m in the horizontal and 1000 m in the vertical. The vertical extent being about twice the horizontal extent allows the model to simulate the interaction between the free atmosphere and the ABL.

Even though the lidar provides data at a 1.5-m resolution in the radial direction, a 2.5-m grid size was chosen in the horizontal x and y directions, based on a trade-off between

accuracy and computing resources. In the vertical direction, a stretched coordinate is used: the first grid point is 0.18 m above the surface to better resolve the surface layer and the largest grid increment near the upper boundary is about 25 m. The total number of grid cells is 225 by 225 by 81 (~ 4.1 million). The time step for the model integration is 0.125 s, to match the ultra-fine vertical resolution near the surface. It takes 50,000 node-hours of CPU time on the 128-node SGI super-clustered Blue Mountain computer at LANL to perform a one-hour model simulation.

All the sub-grid transports use a very small diffusivity coefficient with a constant value of 10^{-7} m^2 s^{-1}. Our ABL simulation is thus similar to direct numerical turbulence simulations at least in terms of the very small grid size near the surface and the small diffusivity coefficient. Margolin et al. (1999) demonstrated recently that a non-oscillatory advection scheme such as the Multidimensional Positive-Definite Advection Transport Algorithm (MPDATA) used in our model can accurately reproduce the dynamics of an atmospheric convective boundary layer without incorporating an explicit sub-grid scale diffusion scheme. Other researchers (e.g., Linden et al., 1994) reached similar conclusions for different flow regimes. It appears that the implicit diffusion built into non-oscillatory advection schemes serves well as an explicit sub-grid scale diffusion module.

The initial state of the model simulation was constructed based on the balloon soundings, ship measurements, and the lidar profiles collected by CSP on 26 March 1996. The

model's initial ABL structure is assumed to be vertically well mixed with a constant water-vapor mixing ratio of 19.5 g kg^{-1} and a potential temperature of 301.5 K. The sea surface temperature is set at 302.5 K and the surface water-vapor mixing ratio at 22.5 g kg^{-1}, based on the surface observations from CSP. To excite an initial disturbance, a random temperature perturbation with a magnitude of 0.01 K is imposed at the surface. The initial momentum field is set to be identically zero. A large-scale subsidence rate of 0.01 cm s^{-1} is prescribed to help maintain the height of the mixed layer. No-slip and cyclic boundary conditions are, respectively, used in the vertical and lateral directions.

We wish to compare the model results directly with the lidar data. Since the model output of any variable at a specific time represents an instantaneous three-dimensional field, it cannot readily be compared with the lidar imagery. We designed a simple visualization code called VIEWER, which mimics the lidar's actual scanning geometry and resolution. It helps us "view" the model output that is generated every 0.75 s. Each modeled line-of-sight in VIEWER is thus extracted from a different instantaneous output file. It represents the data within an angle of 0.5 deg, out to the radial distance of 560 m. To render more faithful the representation of the actual lidar's coverage as a function of radial distance, VIEWER divides each 0.5-deg viewing angle further into ten equal sub-angles. We map next the simulated data from Cartesian onto the polar coordinates given by each modeled sub-line-of-sight, with a radial resolution of 2.5 m. The final image is then plotted back in Cartesian coordinates. Our VIEWER code thus provides an objective comparison between the simulations and the observations from a scanning lidar.

4. Modeled Images

A quasi-stationary state is reached after 10 model hours into the simulation. It is due to the three-way interaction between radiative forcing, large-scale subsidence, and turbulent mixing. The main features of ABL dynamics are well captured by the simulation's quasi-steady state. At hour 10, the mixed layer is, on the average, moister by about 1.5 g kg^{-1} than the initial value, suggesting vigorous moistening caused by the plumes rising from the warm and wet ocean surface. A towering thermal extends from the surface into the free-convection layer, whose top lies for the given model parameters at about 150 m. The entrainment of dryer and warmer air from the free atmosphere, above the first inversion, downward into the mixed layer is also successfully reproduced (not shown).

The HIGRAD simulation results at 12 hr are shown, using the VIEWER visualization procedure, in Fig. 2. Despite the discrepancies between the two figures caused by the different data textures, the simulated structure and variability of the water-vapor plumes are in fair agreement with the observations shown in Fig. 1. Some more detailed comparisons are described in Section 5. The regrouping of the surface-layer plumes into larger moist eddies is clearly simulated in Fig. 2A. The accompanying downward dry eddies that counterbalance the upward mass and momentum fluxes are also well captured. The model, however, appears to produce a larger area of downward dry eddies (Figs. 2A, B) than seen in the observations (Figs. 1A, B). This is due to the cyclic boundary conditions used in the model simulations. Since no in- and outflows are allowed, the net upward and downward mass fluxes are required to balance with each

other. This might impose some effects on the plume simulations as pointed out by Hunt (1999).

Suggested refinements of the Monin-Obuhkov theory for the surface-layer structure include the drying effects of the mixed-layer intrusions (Williams and Hacker, 1993). Our model results (Fig. 2) strongly support the idea that dynamic interactions between the surface layer and the mixed layer are a major mechanism in maintaining the structure of a convective ABL, in good agreement with the lidar observations (Fig. 1).

The HIGRAD-plus-VIEWER system also helps us understand how the transient features may produce aliasing effects in the data images (e.g., Fig. 1) collected from a scanning lidar. By comparing the scanned VIEWER imagery with the instantaneous model output, we found that the overall ABL structure observed through vertical scans (Fig. 2A) does resemble individual snapshots of the modeled ABL. The ABL is characterized, within a typical scanning period, by a gradually evolving upward moist branch (left half of Fig. 2A) and a quasi-stationary downward dry branch (right half of Fig. 2A) that change but little between scans.

More severe aliasing, however, is found in the modeled horizontal scan near the ocean surface, as shown in Fig. 3. Figure 3A shows the modeled imagery of a 90-degree horizontal scan 10 m above the surface, with 81 lines-of-sight in a 60-s scanning time (i.e., an azimuthal resolution that is coarser by a factor of two than in Fig. 2B). Shown in

Figs. 3B–3D are the instantaneous water-vapor fields simulated at 1, 30, and 60 s and included in the VIEWER scanning of Fig. 3A.

The background contrast between wet and dry zones remains the same throughout the 60-s interval. It is dominated by the more persistent larger-scale dynamics, as described previously. At this scale, the spatial-pattern correlations between the vertical-motion field and the water-vapor concentrations are quite high. The distribution of small-scale plumes and their intensity, however, are highly transient within this interval. As a result, the relative plume intensity shown in the modeled lidar imagery (Fig. 3A) is apparently aliased by the plume evolution with time.

The aliasing problem can, in principle, be handled by improving the lidar's performance in terms of increasing the instrument's scanning speed and the power of the laser while maintaining accuracy and coverage. Our numerical experiments show that the small-scale aliasing problem shown above can be considerably remedies, if a 15-s scanning time on the same spatial domain shown in Fig. 3D is used. This agrees with the recycling time scale mentioned earlier and implies that a delay between scans needs to be about 0.2 s.

This problem can also be handled by adding data assimilation capabilities to our integrated system without changing the current instrument's performance. Data assimilation is a numerical approach to combining measurements that are unevenly distributed in space and time with a model that simulates the flow being observed (Daley,

1991). Near-optimal and computationally feasible methods exist to deal with trade-offs between observing pattern and accuracy, like the one at hand (Ghil and Malanotte-Rizzoli, 1991; Ghil et al., 1997).

5. Quantitative Comparison with Lidar Observations

The HIGRAD model simulates the size, frequency, and amplitude of the turbulent microscale water vapor field in the ABL. Therefore we are able to make a quantitative comparison between lidar observations and HIGRAD model results based on an ensemble statistical analysis. The analysis is broken into two parts; the descriptive statistics of selected lidar data and model results, and spatial Fourier analysis of the microscale structural distribution and frequency inherent in the concentration values supporting the images presented in the last section.

A metric for determining whether the values from the two populations are similar is the lidar measurement uncertainty for water vapor since model results do not have accuracy limits associated with it's values. From previous experiments, the absolute accuracy of the lidar when compared to accepted standards is between 10 to 15%, statistics within this uncertainty would be considered indistinguishable from one another (Eichinger et al., 1999). Mixing ratio transects (i.e., averaged mixing ratios as a function of X-range) with an equal number of values were extracted from Figs. 3A (model) and the parent scan of Fig. 1B (lidar) and descriptive statistics were calculated and summarized in Table 1. It appears from the bulk statistics that the two populations are the same. Robust analyses of means and medians indicate that at 95% confidence the lidar data and model values show

no appreciable differences. The two populations differ in their frequency distributions; the lidar is skewed toward higher moisture when compared to the HIGRAD simulation, while the HIGRAD results are more Kurtotic suggesting that the model generates more discrete coherent eddies then observed by the lidar.

The bulk statistics described above do not show how the turbulent structures observed in the lidar measurements and the modeled results compare. To evaluate the size and frequency of turbulent microscale structures, we perform a spatial analysis based on the 1-D Fourier analysis technique, assuming that the turbulent structures can be fit by a sinusoidal waveform (Tennekes and Lumley, 1972). Both data sets were detrended and evaluated with an unevenly-sampled series analysis (Scargle, 1981). The Fourier transform had a tapered cosine window applied to minimize high frequency leakage (Stull, 1988). Periodograms (Fig. 4) were created from the normalized power versus frequency (or wave-number) distribution and 'peak-false-alarm' uncertainty analysis was performed to determine the significance of the periodogram structures (Horne and Baliunas, 1986).

The lidar periodogram (Fig. 4 A) shows three major peaks at 188 m, 34 m, and 27 m. The first peak corresponds to the large-scale exchange effects between the ABL on the surface layer, while the two smaller peaks represent the dominant microscale cellular features, as discussed earlier in this paper. The non-labeled peak adjacent to the 188-m peak may represent the sample domain. The other non-labeled peaks represent less significant noise at smaller scales. The periodiogram for the HIGRAD simulation (Fig.

4B) appears quite similar to Fig. 4A, with the exception that the domain effects are much larger. Also, the large-scale effects of the ABL are on a somewhat smaller scale as shown in the comparison between Fig1. 1B and 2B. It is not surprising to note that the small-scale noise is nearly indistinguishable in the HIGRAD results.

6. Concluding Remarks

We demonstrated here that our integrated model-instrument approach, based on Raman lidar water vapor data and the HIGRAD simulations, could resolve the plume-scale turbulent features associated with water vapor over a warm ocean surface. Our study helps to better understand the degree to which the lidar measurements represent faithfully the atmospheric boundary layer's spatial and temporal features. The lidar water vapor data collected over the Pacific warm pool and the HIGRAD simulations were first compared with each other. The results were then used to identify the potential aliasing effects of lidar measurements. This problem can be handled either by improving the lidar's performance or by adding data assimilation capabilities to our integrated system, or both.

The essence of correctly and robustly parameterizing the surface-air exchange in large-scale climate models is to resolve and describe the scales and mechanisms that govern the surface evaporation. We showed that, over warm ocean surfaces, rate-limiting exchange processes occur in turbulent and convective motions at scales of about 10 meters. The surface plumes and their transport properties are modulated and counterbalanced by

larger dry eddies that penetrate downward from the mixed layer. Existing parameterizations of the surface layer have not yet successfully included these processes, not even by using a curve-fitting approach based on Monin-Obuhkov theory (Brutsaert, 1999). Over land surfaces, near-surface inhomogeneities — due to variable terrain and vegetation — are critical to the variability of water-vapor plumes and to the exchange processes they mediate. This renders fine-scale ABL exploration by the powerful approach described here even more imperative.

Acknowledgments

This research was performed under the auspices of the U.S. Department of Energy (DOE). The Advanced Computing Laboratory at LANL provided the computing support. M.G.'s work was supported under an IGPP/LANL mini-grant for campus-laboratory collaboration.

References

Avissar, R., E. W. Eloranta, K. Gurer, and G. J. Tripoli, An evaluation of the large-eddy simulation option of the regional atmospheric modeling system in simulating a convective boundary layer: A FIFE case study, *J. Atmos. Sci.*, **55**, 1109-1130, 1988.

Brutsaert, W., Aspects of bulk atmospheric boundary layer similarity under free-convective condition. *Rev. Geophys.*, **37**, 439-451, 1999.

Clifford, S. F., J. C. Kaimal, R. J. Lataitis, and R. G. Strauch, Ground-based remote profiling in atmospheric studies: An overview, *Proc. IEEE*, **82**, 313-355, 1994.

Cooper D. I., W. Eichinger, R. Ecke, C.-Y. J. Kao, and J. M. Reisner, 1997. Initial investigations of micro-scale cellular convection in an equatorial marine atmospheric boundary layer revealed by lidar. *Geophys. Res. Lett.*, **1**, 45-48.

Cooper D. I., W. E. Eichinger, S. Barr, W. Cottingame, M. V. Hynes, C. F. Keller, C. F. Lebeda, and D. A. Poling, 1996. High resolution properties of the equatorial Pacific marine atmospheric boundary layer from lidar and radiosonde observations. *J. Atmos. Sci.*, **53**, 2054-2075.

Cooper, D. I., W. E. Eichinger, D. Hof, D. Jones, C. R. Quick, and J. J. Tiee, Observations of coherent structures from a scanning lidar. *Agric. Forest Meteorol.*, **67**, 137-150, 1994.

Daley, R., *Atmospheric Data Analysis*, 420 pp., Cambridge Univ. Press, Cambridge,1992.

Eichinger, W. E., D. I. Cooper, P. Forman, J. Griegos, M. Osborne, D. Richter, L. Tellier, and R. Thornton, The development of a scanning Raman water-vapor lidar for boundary llayer and tropospheric observations. *Atm. Oceanic Tech*., **16**, 1753-1766.

Eichinger, W. E., D. I. Cooper, F. L. Archuleta, D. Hof, D. B., Holtkamp, R. R. Karl, C. R. Quick, and J. J. Tiee, Development of a scanning solar blind water water Raman-lidar. *Appl. Opt*., **33**, 3923-3932, 1994.

Eloranta, E. W., and D. K. Forrest, Volume-imaging lidar observations of the convective structure surrounding the flight path of a flux-measuring aircraft. *J. Geohpys. Res.,* **97**, 18383-18393, 1992.

Ghil, M., and P. Malanotte-Rizzoli, Data assimilation in meteorology and oceanography, *Adv. Geophys.*, **33**, 141–266, 1991.

Ghil, M., K. Ide, A. F. Bennett, P. Courtier, M. Kimoto, and N. Sato (Eds.), 1997: *Data Assimilation in Meteorology and Oceanography: Theory and Practice*, Meteorological Society of Japan and Universal Academy Press, Tokyo, 496 pp.

Hagelberg, C. R., D. I. Cooper, C. L. Winter, and W. E. Eichinger, Scale properties of microscale convection in the marine surface layer, *J. Geophys. Res.*, **103**, 16897-16907, 1998.

Horne, J.H., and Baliunas, S.L., A prescription for period analysis of unevenly sampled time series. *The Astrophys. J.* **302**:757-763, 1986.

Hunt, J. C. R., Eddy dynamics and kinematics of convective turbulence. In *Buoyant Convection in Geophysical Flows.* Edited by Plate et al., Kluwer Academic Pub., 41-82, 1999.

Kao, C.-Y. J., Y. H. Hang, D. I. Cooper, W. S. Smith, J. M. Reisner, and W. E. Eichinger, High resolution modeling of lidar data: Mechanisms governing surface water vapor during SALSA. *Agric. Forest Meteorol.*, **105**, 185-194.

Kaimal, J. C., and J. J. Finnigan, *Atmospheric Boundary-Layer Flows: Their Structure and Measurement*, 289 pp., Oxford University Press, 1994.

Khanna, S., and J. G. Brasseur, Three-dimensional buoyancy- and shear-induced local structure of the atmospheric boundary layer, *J. Atmos. Sci*., **55**, 710-743, 1998.

Lawford, R., 1996. Some scientific questions and issues for the GEWEX Continental-scale International Project (GCIP) research community. 2nd International Sci. Conf. on Global Energy and Water Cycle, June 17-21, Washington DC, 162-167.

Linden, P. F., J. M. Redondo, and D. L. Youngs, Molecular mixing in Rayleigh-Taylor instability. *J. Fluid. Mech.*, **265**, 97-124.

Mahrt, L., 1998, Flux sampling errors for aircraft and towers. *J. Atmos. Ocean. Tech.*, **15**, 416-429.

Margolin, L., P. K. Smolarkiewicz, and Z. Sorbjan, Large-eddy simulations of convective boundary layers using nonoscillatory differencing. *Physica D*, **133**, 390-397,1999.

Melfi, S. H., J. D. Lawrence, and M. P. McCormick, Observations of Raman scattering by water vapor in the atmosphere. *Appl. Phys. Lett.*, **15**, 295-297, 1969.

Post, M. J., C. W. Fairall, J. B. Snider, Y. Han, A. B. White, W. L. Ecklund, K. M. Weickmann, P. K. Quinn, D. I. Cooper, S. M. Sekelsky, R. E. McIntosh, P. Minnett, and R.O. Knuteson, The Combined Sensor Program: An air-sea science mission in the central and western Pacific Ocean. *Bull. Amer. Meterol. Soc.*, **78**, 2797-2815, 1997.

Ramanathan, V., and W. Collins, Thermodynamic regulation of ocean warming by cirrus clouds deduced from the 1987 El Nino. *Nature*, **351**, 27-32, 1991.

Scargle, J.D., Studies in astronomical time series analysis I.. Modeling random processes in the time domain. *The Astrophys. J. Supp. Series* **45**:1-71, 1981.

Smith, W. S., and C.-Y. J. Kao, Numerical simulations of stratiform clouds observed in 1987 FIRE IOP with the emphasis on diurnal variation. data. *Mon. Wea. Rev*., **8**, 1803-1816, 1996.

Smolarkiewicz, and L. G. Margolin, On forward-in-time differencing for fluids: Extension to a curvilinear framework. *Mon. Wea. Rev*., **121**, 1847-1859, 1993.

Smolarkiewicz, P. K. and L. G. Margolin, MPDATA: A finite-difference solver for geophysical flows. *J. Comput. Phys*., **140**, 459-480, 1998.

Stull, R. B., *An Introduction to Boundary Layer Meteorology*, 666 pp., Kluwer Academic Pub., 1988.

Tennekes, H. and Lumley, J.L., *A First Course in Turbulence*, 300 pp., The MIT Press,

Williams, A. G., J. M. Hacker, Interactions between coherent eddies in the lower convective boundary layer, *Boundary-Layer Meteorol*., **64**, 55-74.

Wyngaard, J. C., Convective processes in the lower atmosphere, in *Flow and Transport in the Natural Environment: Advances and Applications*, edited by W. L. Steffen and O. T. Denmead, pp. 240-260, Springer-Verlag, 1988.

Figure Captions

Fig.1. Lidar data collected during CSP: (A) A portion of a vertical Raman lidar scan of water-vapor mixing ratio acquired on 26 March 1996 at 0420 UTC (1820 local time), with horizontal distance on the abscissa and height above sea level (ASL) on the ordinate. The scan reveals near-surface small-scale convective plumes (in red), as well as organized upward (in red, yellow, and green) and downward eddies (in purple and blue). (B) A portion of a horizontal Raman lidar scan of water-vapor mixing ratio acquired at 10 m above the ocean surface on 26 March 1996 at 0440 UTC (1840 local time). The *x*– and *y*–axes are two perpendicular directions in the horizontal. Sinking air with low water-vapor concentration surrounds isolated convective plumes. Color bars are shown below each panel.

Fig. 2. Same as Fig.1, except for model results from the HIGRAD and VIEWER codes. The simulated scans are from the *x*-axis toward the *y*-axis, as in Fig. 1. The two panels are both derived from the same one-minute chunk of model output taken 12 hr after the initial time, while the two panels from Fig. 1 were, by necessity, 20 minutes apart.

Fig. 3. (A) is the modeled horizontal scan with a coarser resolution in azimuth but for a larger scanned area in comparison with Fig. 2B; (B), (C), and (D) are the instantaneous water-vapor fields at 1 s, 30 s, and 60 s, respectively, into the scanning interval used in Fig. 3D. The color legends are the same as in Fig. 2B.

Fig. 4. Periodograms for (A) lidar observations and (B) HIGRAD simulations, based on the parent scan of Fig. 2B and Fig. 3A, respectively.

STATISTIC	**LIDAR**	**HIGRAD**
Sample Size	372	372
Sum	6823	6801
Maximum	19.69	19.69
Minimum	17.66	17.65
Range	2.03	2.04
Mean	18.34	18.28
Standard Deviation	0.49	0.45
Variance	0.24	0.20
Standard Error	0.03	0.02
Median	18.10	18.20
Skewness	0.87	0.52
Kurtosis	-0.24	-0.62

Table 1. Descriptive statistics for lidar and HIGRAD water vapor mixing ratios averaged over the Y-range.

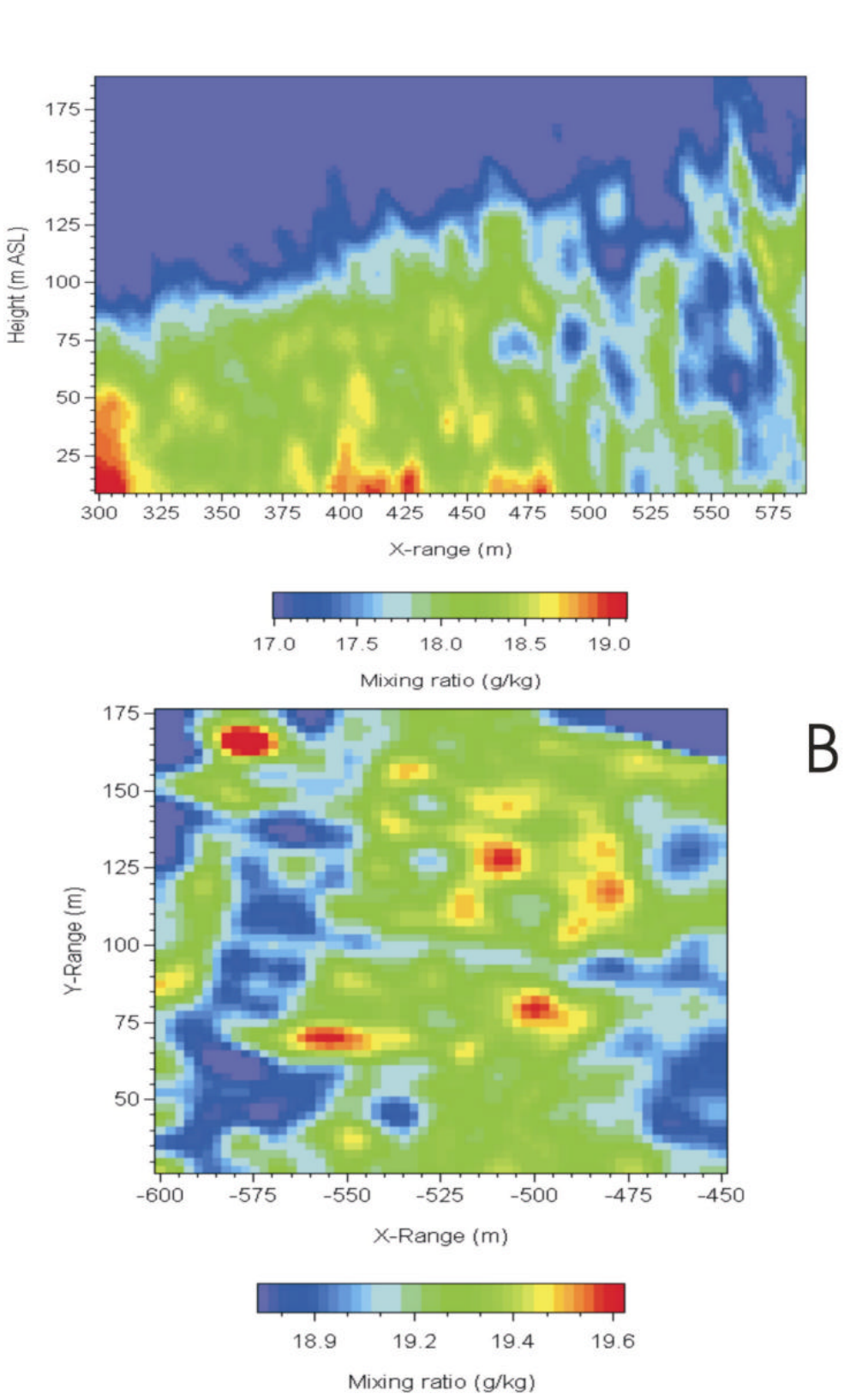
A
Height (m ASL)
175
150
125
100
75
50
25
300 325 350 375 400 425 450 475 500 525 550 575
X-range (m)
17.0 17.5 18.0 18.5 19.0
Mixing ratio (g/kg)
B
Y-Range (m)
175
150
125
100
75
50
-600 -575 -550 -525 -500 -475 -450
X-Range (m)
18.9 19.2 19.4 19.6
Mixing ratio (g/kg)

Fig. 1

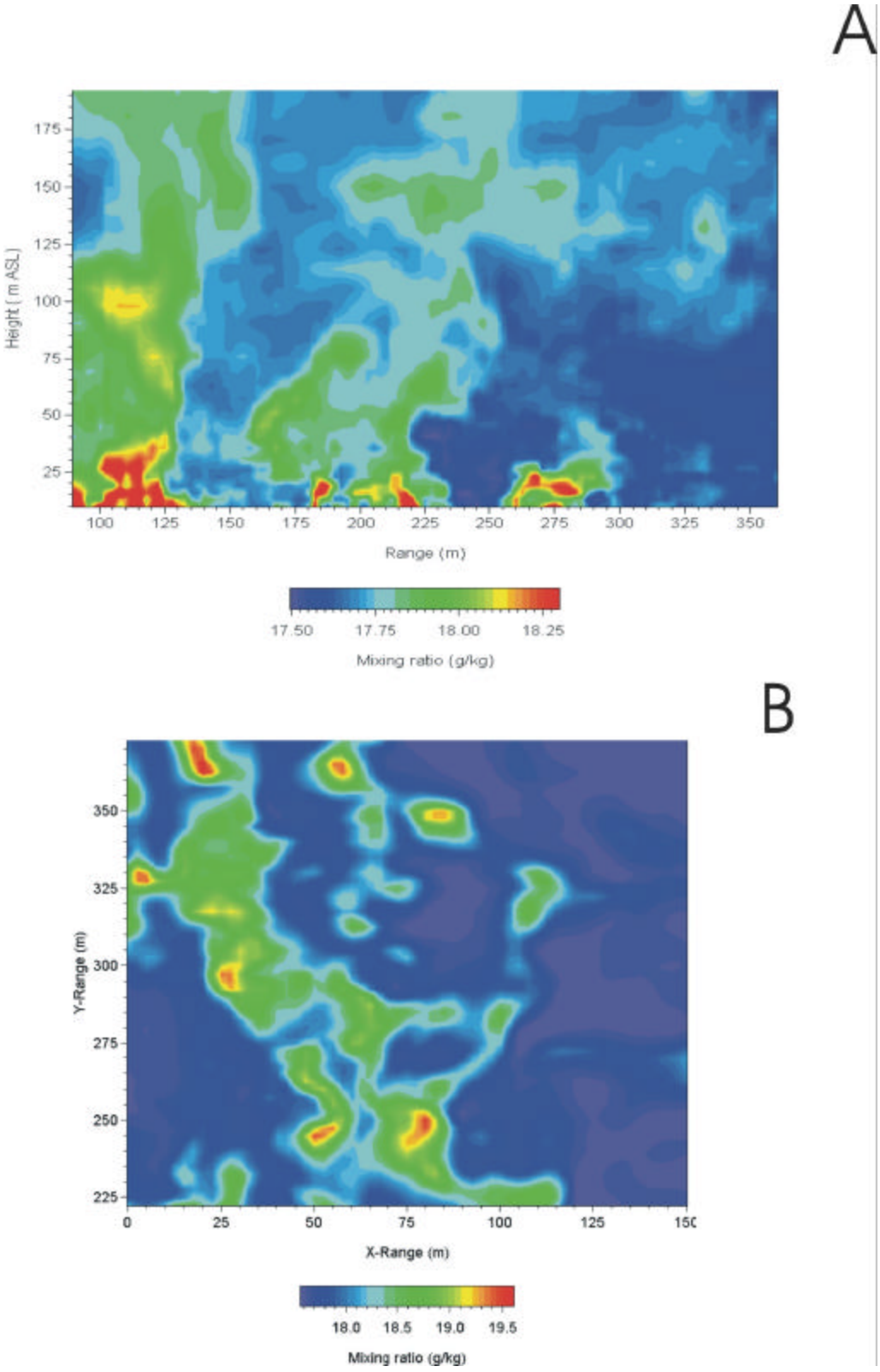
A
Height (m ASL)
175
150
125
100
75
50
25
100 125 150 175 200 225 250 275 300 325 350
Range (m)
17.50 17.75 18.00 18.25
Mixing ratio (g/kg)
B
Y-Range (m)
350
325
300
275
250
225
0 25 50 75 100 125 150
X-Range (m)
18.0 18.5 19.0 19.5
Mixing ratio (g/kg)

Fig. 2

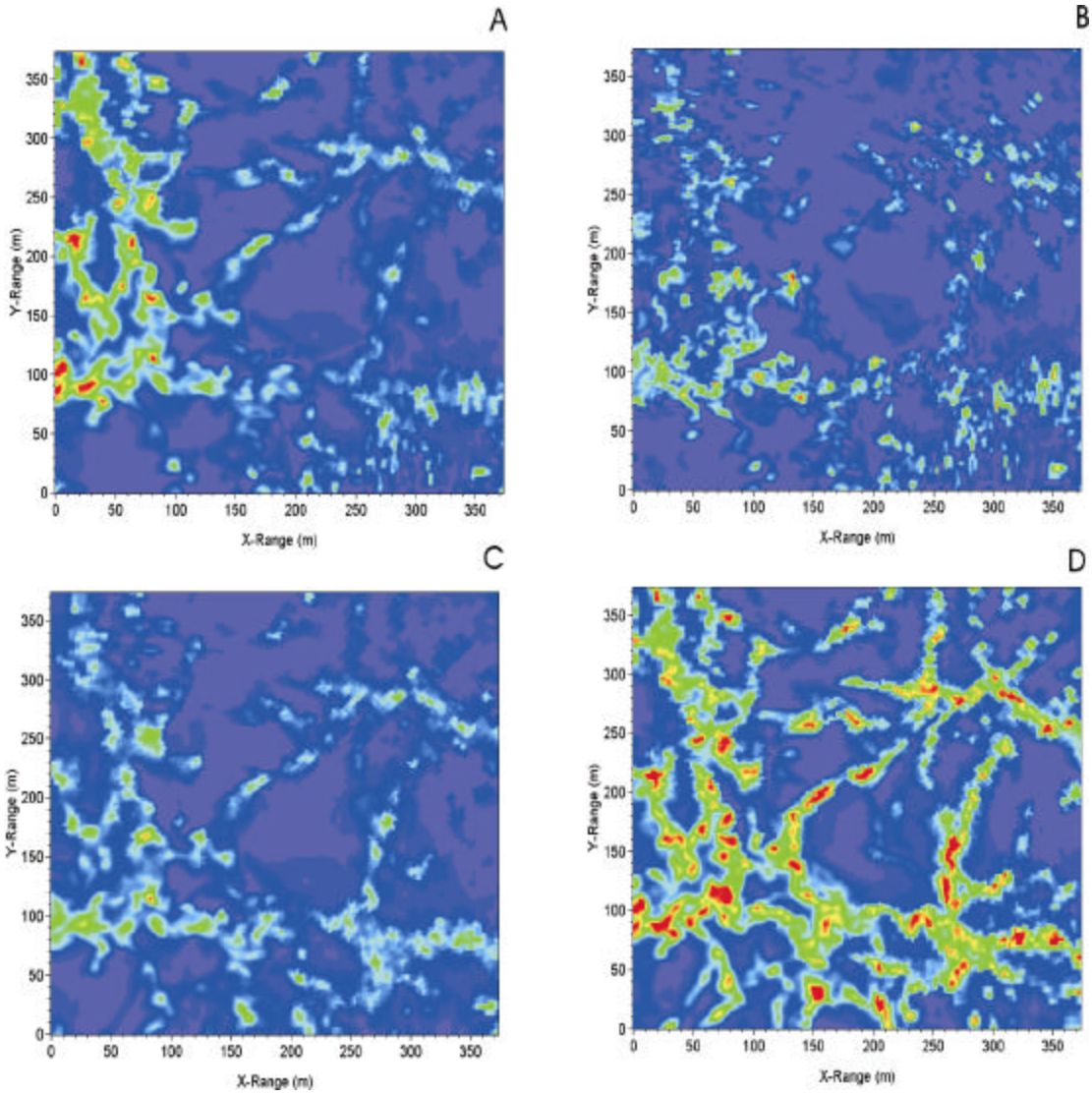

Fig. 3